

# Revisiting *LS I +61°303* with VLBI astrometry

Y. W. Wu<sup>1,2\*</sup>, G. Torricelli-Ciamponi<sup>3</sup>, M. Massi<sup>4,†</sup>, M. J. Reid<sup>5</sup>, B. Zhang<sup>6</sup>, L. Shao<sup>7</sup>, X. W. Zheng<sup>8</sup>

<sup>1</sup> National Astronomical Observatory of Japan, Osawa 2-21-1, Mitaka, Tokyo 181-8588, Japan

<sup>2</sup> National Time Service Center, Key Laboratory of Precise Positioning and Timing Technology, Chinese Academy of Sciences, Xi'an 710600, China

<sup>3</sup> INAF - Osservatorio Astrofisico di Arcetri, L.go E. Fermi 5, Firenze, Italy

<sup>4</sup> Max-Planck-Institut für Radioastronomie, Auf dem Hügel 69, 53121 Bonn, Germany

<sup>5</sup> Harvard-Smithsonian Center for Astrophysics, 60 Garden Street, Cambridge, MA 02138, USA

<sup>6</sup> Shanghai Astronomical Observatory, 80 Nandan Road, Shanghai 20030, China

<sup>7</sup> Max Planck Institute for Gravitational Physics (Albert Einstein Institute), Am Mühlenberg 1, D-14476 Potsdam-Golm, Germany

<sup>8</sup> School of Astronomy and Space Sciences of Nanjing University, Nanjing 210093, China

Last updated 2017 April 15

## ABSTRACT

We conducted multi-epoch VLBA phase reference observations of *LS I +61°303* in order to study its precessing radio jet. Compared to similar observations in 2006, we find that the observed elliptical trajectory of emission at 8.4 GHz repeats after the 9-year gap. The accurate alignment of the emission patterns yields a precession period of  $26.926 \pm 0.005$  d, which is consistent with that determined by Lomb-Scargle analysis of the radio light curve. We analytically model the projection on the sky plane of the peak position of a precessing, synchrotron-emitting jet, which traces an elliptical trajectory on the sky. Comparing the simulation with the VLBA astrometry we improve our knowledge of the geometry of the system. We measure the *LS I +61°303* absolute proper motion to be  $-0.150 \pm 0.006$  mas yr<sup>-1</sup> eastward and  $-0.264 \pm 0.006$  mas yr<sup>-1</sup> northward. Removing Galactic rotation, this reveals a small,  $< 20$  km s<sup>-1</sup>, non-circular motion, which indicates a very low kick velocity when the black hole was formed.

**Key words:** radio continuum: stars – Stars: jet – X-rays: binaries – X-rays: individuals: *LS I +61°303* — gamma rays: star — astrometry

## CONTENTS

- 1 Introduction
  - 2 The precessing jet in *LS I +61°303*
  - 3 Observation and Data reduction
  - 4 precession period
  - 5 Modeling the astrometry of the jet core
    - 5.1 The orbital motion
    - 5.2 The jet precession motion
    - 5.3 The total motion: results
  - 6 Proper motion and 3D motion
  - 7 Conclusions
- Acknowledgements

## 1 INTRODUCTION

*LS I +61°303* is an unusual high-mass x-ray binary (HMXB). It was discovered as a periodic radio source by Gregory & Taylor (1978) and later periodic variations in X-ray (Paredes et al. 1997; Eikenberry et al. 2001) and  $\gamma$ -ray (Albert et al. 2009) were observed. The origin of its  $\gamma$ -ray, X-ray, optical/infrared and radio emission has been debated for decades (Taylor et al. 1992; Marti & Paredes 1995; Bosch-Ramon et al. 2006; Romero et al. 2007; Massi et al. 2013). The X-ray characteristics of *LS I +61°303* fit those of accreting black holes at moderate luminosity (Massi et al. 2017) that would make this source along with MWC 656, the only systems where a black hole accretes from the wind of a Be companion star.

Kaufman Bernadó et al. (2002) suggested *LS I +61°303* is a precessing microblazar, a kind of microquasars where precession periodically brings the approaching jet close to the line of sight and Doppler boosting its emission. Very Long Baseline Array (VLBA) astrometry in 2006 provided the first estimate of the precession period. In order to study the properties of the precessing jet, we conducted a second set of multi-epoch VLBA phase-reference observations in 2015. Section 2 summarizes previous radio observations of *LS I +61°303* and the precessing scenario. We describe the new observations and data reduction in Section 3. In Section 4 we

\* yuanwei.wu@ntsc.ac.cn

† mmassi@mpifr-bonn.mpg.de

present a joint analysis of 2006 and 2015 VLBA datasets, which indicates a very stable precession of LS I +61°303 and allows us to determine an accurate precession period. In Section 5 we present our theoretical astrometry model. In Section 6, we discuss the measured 3-dimensional motion of LS I +61°303. Section 7 presents our conclusions.

## 2 THE PRECESSING JET IN LS I +61°303

A Lomb-Scargle timing analysis of 36.8-yr radio observations (Massi & Torricelli-Ciamponi 2016) confirmed previous discoveries (e.g., Massi et al. 2015) of two characteristic periods,  $P_1 = 26.496 \pm 0.013$  d and  $P_2 = 26.935 \pm 0.013$  d, in the emission from LS I +61°303 (see Fig. 1). The period  $P_1$  corresponds to orbital periodicity (Gregory 2002). Several authors (Taylor et al. 1992; Marti & Paredes 1995; Bosch-Ramon et al. 2006; Romero et al. 2007; Jaron et al. 2016) have shown that because of the high eccentricity ( $e = 0.7$ , Casares et al. (2005)) there are two accretion peaks along the orbit of LS I +61°303: one close to periastron and a second one shifted towards apastron. Near periastron the ejected relativistic particles encounter the strong stellar radiation field of the B0 star and suffer strong inverse-Compton (IC) losses and, thus, do not produce a radio outburst. However, for the second accretion peak near apastron, the IC losses are smaller and synchrotron emission in the radio band is observed (Taylor et al. 1992; Marti & Paredes 1995; Bosch-Ramon et al. 2006; Romero et al. 2007; Jaron et al. 2016).

The second feature in the spectrum of Fig. 1, at  $P_2 = 26.935 \pm 0.013$  d, was more challenging to understand. The simplest explanation is that the observed flux density from a relativistic jet (Mirabel & Rodríguez 1999) is the product of an intrinsically variable jet and Doppler boosting toward the observer:  $S_{\text{observed}} = S_{\text{intrinsic}}(f(P_1)) \times DB$ , where  $DB$  is the Doppler boosting factor. Massi & Torricelli-Ciamponi (2014) suggested that the  $DB$  factor could be a function of  $P_2$ .

The observations indeed support a variation of the jet angle. European VLBI Network (EVN), MERLIN and VLBA images show not only a jet at different position angles, but in addition the jet is sometimes double-sided (Massi et al. 2012, and references therein, but see Dhawan et al. (2006) for interpretations with pulsar wind model). One-sided jet structures are seen in blazars, because of their small angle with respect to the line of sight, counter-jet emission is de-boosted below detection sensitivity. The switch in LS I +61°303 between a two-sided and a one-sided structure indicates that precession bringing the jet to small angles with respect to the line of sight. The radio images confirm therefore a variation of the angle between jet and line of sight and indicate that rather small jet to line-of-sight angles are reached. Information on periodicity came from 2006 astrometry (Dhawan et al. 2006). Massi et al. (2012) showed as the peak of the images, associated with the jet core, described an ellipse path on the sky over 27–28 d, i.e., close to  $P_2$ . In the following sections we present new observations and we compare the astrometry data from 2006 and 2015 with the predictions of a precessing jet model.

## 3 OBSERVATION AND DATA REDUCTION

We conducted 10-epochs of phase-referenced observations with the VLBA from 2015 July 24 to August 23, spanning one orbital cycle of the binary with roughly 3-d intervals. At each epoch observations

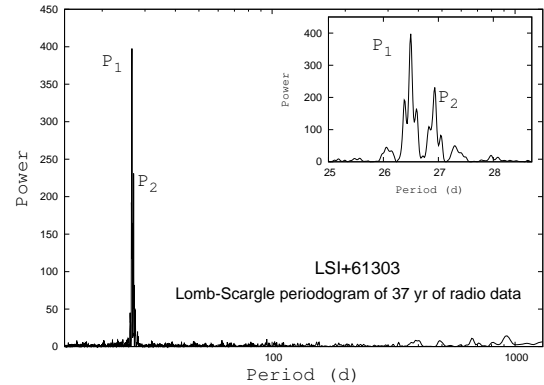


**Figure 1.** Lomb-Scargle periodogram of LSI+61303 with zoom of the spectral window 25–29 d around  $P_1$  and  $P_2$ .

spanned 4 hours. The angular separation between LS I +61°303 and the calibrator, J0244+6228, is 1.3°. The antenna switch time, i.e., one phase-referencing cycle of the calibrator J0244+6228 and LS I +61°303 is 3 min. The total on-source times for LS I +61°303, J0244+6228 and the astrometric check source, J0239+6005, were 2.0, 1.2 and 0.5 hours, respectively. The synthesized beams were 2.2×1.0 mas at a position angle of 0° (East of North) for all epochs, except for epoch D for which the MK and NL antennas were unavailable and the synthesized beam was 2.4×1.0 mas at position angle of 51°. We used identical frequency setups as were used for the 2006 VLBA observations: continuum emission at 8.4 GHz, was recorded with four adjacent dual circular polarization intermediate frequency (IF) bands of 16 MHz and correlated with 64 channels per IFs.

The 2006 and 2015 datasets were calibrated using Astronomical Image Processing System (AIPS)<sup>1</sup> together with scripts written in ParselTongue, a python interface to AIPS and Orbit (Kettenis et al. 2006). We first corrected the data for residual delays from Earth orientation parameters (EOP) and ionosphere (TECOR); amplitudes were adjusted for digital sampling corrections (ACCOR), system temperatures and antenna gains; manual phase-calibration was applied to correct for delay offsets between sub-bands. After these procedures, the phase-reference source, J0244+6228, was imaged and self-calibrated using the procedure Muppet in DIFMAP (Pearson et al. 1994; Shepherd 1997). Then the self-calibrated J0244+6228 images of individual epochs were read back into AIPS and served as a model to calibrate delay, rate and phase with FRING. The structure of J0244+6228 appeared stable throughout both the 2006 and 2015 sessions. The self-calibration solutions were then interpolated to the LS I +61°303 and J0239+6005 scans; the latter source was used as an astrometric check. Finally, phase-referenced images were produced by IMAGR. The peak positions of LS I +61°303, which is neither Gaussian-like nor symmetric, were determined from the brightest pixels (of size 0.05 mas×0.05 mas) with IMSTAT by following the approach of Massi et al. (2012).

In Figure 2, we present the astrometry obtained for the check source J0239+6005 relative to the phase-reference source

<sup>1</sup> AIPS is a NRAO software package to reduce radio interferometric data that can be available from <http://www.aips.nrao.edu>

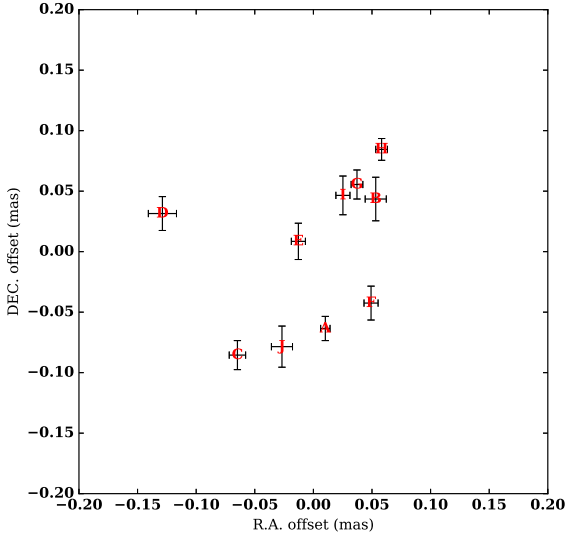


**Figure 2.** Astrometric accuracy of J0239+6005. Red characters denote epochs. The standard deviation is 0.05 mas. The error bars are formal position errors of J0239+6005 determined by 2-D Gaussian fitting of brightness distribution of the phase-reference images with AIPS task JMFIT.

J0244+6228 from the 2015 VLBA observations. We used the AIPS task JMFIT to fit positions and the formal errors are  $\sim 0.008$  mas and  $\sim 0.015$  mas in R.A. and Dec. directions, respectively. The standard deviation of these positions are 0.05 mas in both R.A. and Dec directions<sup>2</sup>. Table 1 lists the jet-core positions of LS I +61°303 from the 2006 and 2015 sessions and the estimated orbital, precessing and long beating phases.

#### 4 PRECESSION PERIOD

In Figure 3, we show the phase reference images of LS I +61°303 in 2006 and 2015, with observation dates labeled. Changes of jet position angles can be clearly seen in both sessions. In most epochs, the jet appears one-sided; however, in epochs of 06JUL03, 06JUL24 and 15JUL24, there are two-side morphologies. This phenomenon can be explained by precession of the jet axis, as illustrated in Figure 7 of [Massi & Torricelli-Ciamponi \(2014\)](#), especially when the angle between the line-of-sight and the jet axis is minimized and Doppler boosting is maximized.

The apparent motions of the jet core can be attribute to four components: (1) orbital motion of  $\approx 0.2$  mas, (2) jet precession of  $\approx 2.5$  mas, (3) proper motion of  $\approx 4$  mas in 9 years and (4) parallax changes of  $\approx 0.2$  mas. Orbital motion and precession at the jet core's position will be discussed in detail in Section 5. The apparent motion caused by the source's parallax can be well modeled since its distance of 2 kpc is known. In the left panel of Figure 4, we show the astrometric results with the parallax component removed, where the reference coordinates (ie, the zero point) are 02h40m31s.6645, 61d13m45s.594 (J2000). In both the 2006 and 2015 sessions, one can see the elliptical trajectory. We align the two ellipses by fitting the jet-core positions shown in the left panel of Figure 4 with seven parameters ( $x_1, y_1, x_2, y_2, a, b, \Theta$ ), where

$(x_1, y_1)$  and  $(x_2, y_2)$  are centers of two ellipses,  $a, b$  and  $\Theta$  are the long/short axes and the position angle of the long axis. (The best fitting values of these parameters, respectively, are  $0.87 \pm 0.04$  mas,  $0.31 \pm 0.05$  mas,  $-2.23 \pm 0.07$  mas,  $-2.08 \pm 0.03$  mas,  $1.39 \pm 0.05$  mas,  $0.48 \pm 0.11$  mas, and  $-43.63 \pm 1.64$  deg). Note, we have assumed an identical elliptical shape for the two sessions, with the only difference being the central positions. The right panel from Figure 4 shows the relative positions of the jet cores referred to the elliptical centers in 2006 and 2015 sessions. One can see that the 2006 and 2015 astrometric data can be well modeled by the source proper motion (see Section 6) and two identical elliptical trajectories caused by jet precession.

We then determine the precession period by aligning the phase of these two ellipses. The ellipse in polar coordinates can be denoted as

$$r = \frac{a \times b}{\sqrt{a^2 \sin^2(\theta - \Theta) + b^2 \cos^2(\theta - \Theta)}} \quad (1)$$

where the reference point is the elliptical center, the reference direction is the east direction,  $a, b$  and  $\Theta$  are the long/short axes and the position angle of the long axis. The polar coordinates  $r$  and  $\theta$  can be converted to the Cartesian coordinates  $x$  and  $y$  using trigonometric functions

In Figure 5, we present  $\theta, x$  and  $y$  vary with time, where  $\Delta t = t - t_{\text{ref}}$ . We assume an identical precessing phase at the reference time,  $t_{\text{ref}}$ . For 2006 and 2015 sessions, we set  $t_{\text{ref}} = t[2006\text{-A}]$  and  $t_{\text{ref}} = t[2015\text{-B}] - \Delta T$ , respectively. Here the  $\Delta T$  is the parameter that we need to estimate.

In the left panel of Figure 5, the dash line is an empirical relationship between  $\Delta t$  and  $\theta$ , that is a monotonic polynomial fitted using data of 2006 sessions.

$$\theta(\Delta t) = a + b \times \Delta t + c \times \Delta t^3 + d \times \Delta t^5 \quad (2)$$

Here we used an odd order polynomial (i.e., with diagonal symmetry rather than mirror symmetry for an even order). The 5th order polynomial was adopted, as it produced much smaller scatter than a 3rd order polynomial and a 7th order polynomial did not yield significant improvement. The dash lines in the middle and right panels then can be determined with equation (1)-(2).

The best  $\Delta T$ , can be estimated as the maximum of the probability density function (PDF), which is defined as

$$\text{Prob} \propto \prod_{i=1}^N \frac{1}{\sigma \sqrt{2\pi}} e^{-\Delta_i^2 / 2\sigma^2} \quad (3)$$

where,

$$\Delta_i^2 = (x_i[\text{obs}] - x_i[\text{model}])^2 + (y_i[\text{obs}] - y_i[\text{model}])^2 \quad (4)$$

are residuals (data minus model);  $\sigma$  was estimated from the post-fit residuals from

$$\sigma^2 = \sum_{i=1}^N \frac{\Delta_i^2}{N}. \quad (5)$$

In Figure 6, we show the PDF for  $\Delta T$ , from which we estimate  $\Delta T = 0.98 \pm 0.63$  d. The PDF is calculated with a step of 0.1 d.

The time interval between 2006-A and 2015-B is 3312.9174 d, take into account  $\Delta T = 0.98 \pm 0.63$  d, the time interval between these two precessing cycles are  $3311.9 \pm 0.6$  d. We can determine the precessing period, once the cycle number between these two periods is known. Meanwhile, if we assume the relation  $P_{\text{long}}$

<sup>2</sup> The R.A. offsets in the Figure are  $\Delta \text{R.A.} \times \cos(\text{DEC})$ .

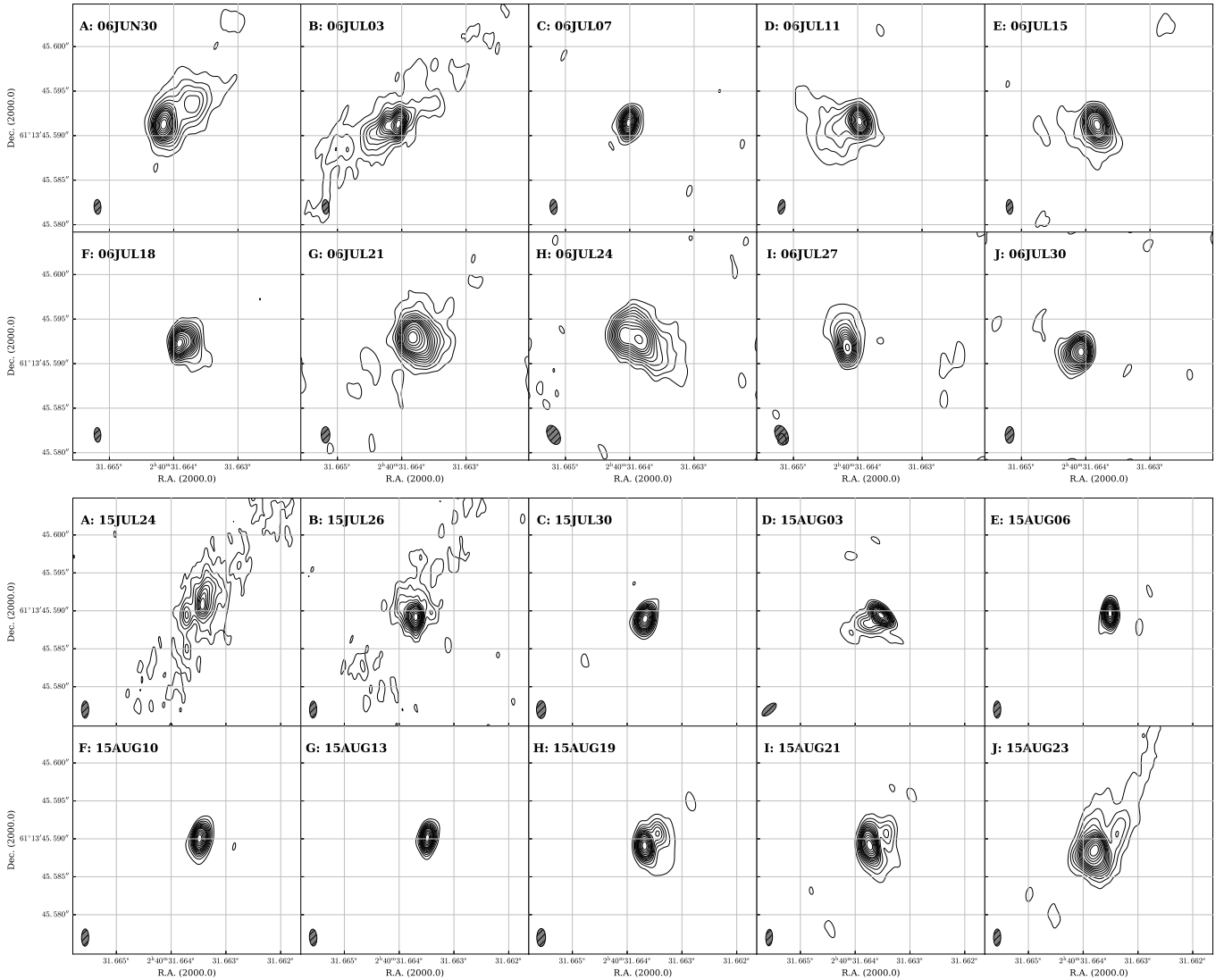


**Figure 3.** Phase reference images of LS I +61°303 in 2006 and 2015 observations. The observational dates are labeled in the top left corner. The hatched grey areas in the bottom left corner denote the synthesized beams. All contour levels start from  $5\sigma$ , and increase with step of  $5\sigma$  (here  $\sigma$  is the rms noise level of the image, which typically was  $0.1 \text{ mJy beam}^{-1}$ ).

$= P_1 \times P_2 / (P_2 - P_1)$  holds (e.g., [Massi & Torricelli-Ciamponi 2016](#)), then we can calculate  $P_{\text{long}}$ , once  $P_1$  and  $P_2$  are given. In upper and lower panels of Figure 7, we present  $P_2$  and  $P_{\text{long}}$  estimated via Monte Carlo simulations, assuming there are 122, 123 and 124 cycles over the time interval of  $3311.9 \pm 0.6 \text{ d}$ . In Figure 7, the red solid/dashed lines indicate  $P_2 = 26.935 \pm 0.013 \text{ d}$  ([Massi & Torricelli-Ciamponi 2016](#)), and  $P_{\text{long}} = 1667 \pm 8 \text{ d}$  ([Gregory 2002](#)). It can be seen that only 123 cycles can produce consistent  $P_2$  and  $P_{\text{long}}$  values. With the value of 123 cycles, we determined an accurate  $P_2$ ,

$$P_2 = (3311.9 \pm 0.6) / 123 = 26.926 \pm 0.005 \text{ d} . \quad (6)$$

## 5 MODELING THE ASTROMETRY OF THE JET CORE

The emissions of LS I +61°303 from  $\gamma$ -rays, X-rays, optical/infrared, and radio wavelengths have been modeled by several authors ([Taylor et al. 1992](#); [Marti & Paredes 1995](#); [Bosch-Ramon](#)

[et al. 2006](#); [Romero et al. 2007](#); [Massi & Torricelli-Ciamponi 2014](#)) in the context of accretion onto a compact object along an eccentric orbit. Observational evidence, especially from measurements of the radio spectral index ([Massi & Kaufman Bernadó 2009](#)) and a high energy double-peak light curve ([Jaron et al. 2016](#)) favors a microquasar rather than a pulsar wind origin ([Dhawan et al. 2006](#)). [Massi & Torricelli-Ciamponi \(2014\)](#) developed a model of a precessing conical jet which emits synchrotron radiation to explain the radio light curve. In this section, we integrate their radiation transfer model in order to simulate observations on the sky plane. For an optically thin jet, the maximum of the emission is at the jet base, while for an optically thick jet the maximum will be displaced down the jet where optical depth unity is achieved. The displacement of the observed radio peaks on the sky plane is due to the emitting plasma changing position owing to the orbital motion of the compact object around the primary star and to the jet precession. In this section, we first examine the two effects separately and then we derive the full jet motion as it appears on the sky.

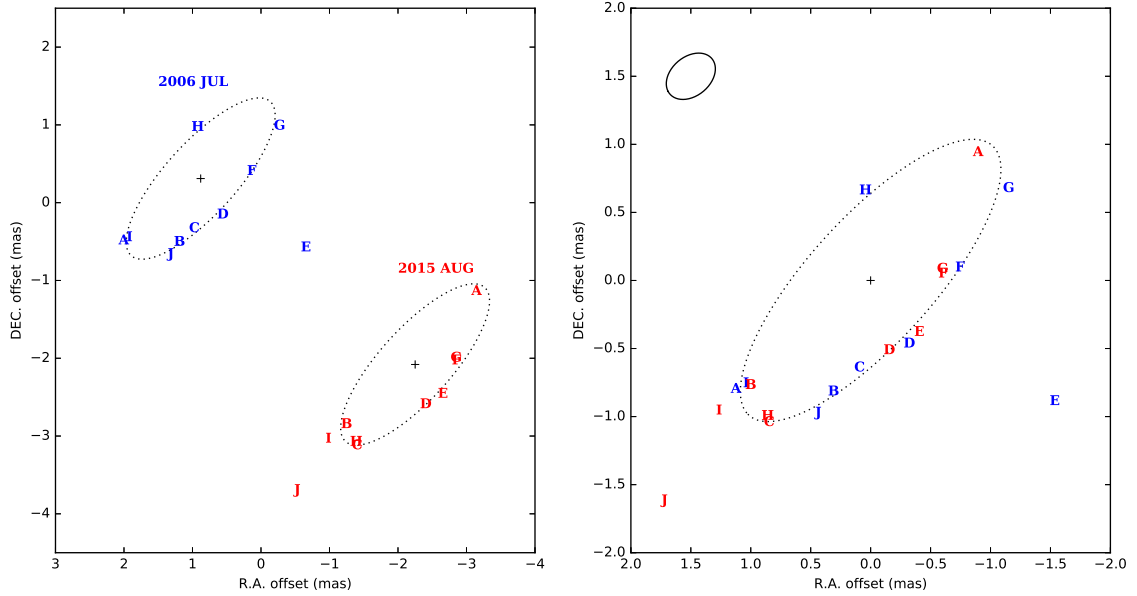


**Figure 4.** *Left panel:* Astrometric results of 2006 and 2015 VLBA observations, with parallax motions removed. Blue characters denote jet peaks in 2006, and red characters denote jet peaks in 2015. The reference coordinate (zero point) is 02h40m31s.6645, 61d13m45s.594. *Right panel:* Same as left panel, but with centers of the two ellipses overlaid. The solid ellipse in the top left corner indicates the scale of the orbit, with a semimajor axis of 0.22 mas (Massi et al. 2012).

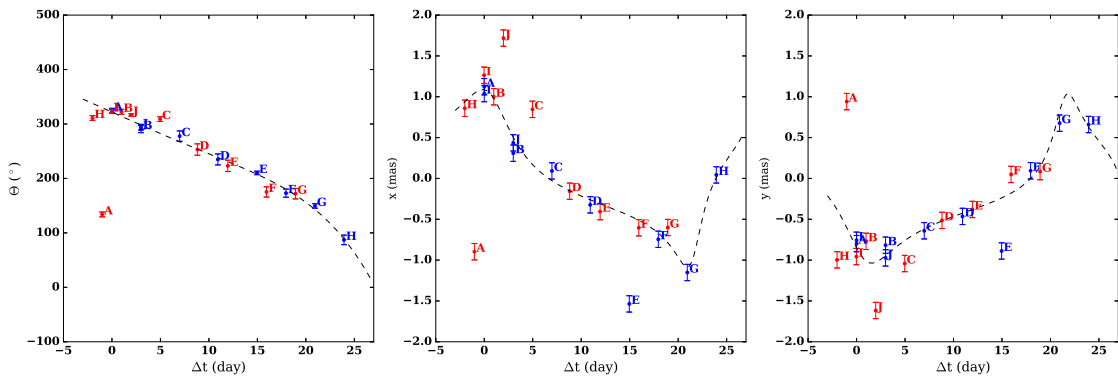


**Figure 5.** Left, middle and right panels are the position angle  $\theta$ ,  $x = \Delta R.A.$  and  $y = \Delta Dec.$  of jet core versus time, respectively. Blue/red characters and dots with error bars denote 2006/2015 observations.

### 5.1 The orbital motion

In Massi & Torricelli-Ciamponi (2014) model, the base of the jet is anchored to the compact object and, hence, follows the compact object along its orbit; this path is drawn as a green ellipse in Fig. 8. The orbit plane forms an angle  $\zeta$  with respect to the plane perpendicular to the line-of-sight.

The system of reference in the orbital plane is at the center of mass of the system i.e. the point  $O$ . The  $y'$  axis is defined by the intersection of the orbital plane and the plane perpendicular to the line-of-sight, with the  $x'$  axis perpendicular to the  $y'$  axis at  $O$ . In this way a rotation of the system  $[x', y']$  around  $[y']$  by an angle  $\zeta$  defines the system of reference  $[x'', y'']$  in the plane perpendicular

to the line-of-sight. In order to parameterize the orientation of the ellipse in the orbital plane we introduce the angle  $\omega$ , which defines the ellipse rotation with respect to the Cartesian system  $[x', y']$  previously defined. See Fig. 8 for angle definitions.

The compact object moves at a distance  $\rho$  from the origin of coordinates. In the plane of motion, the vector radius can be expressed in terms of the ellipse semi-major axis,  $a$ , ellipse eccentricity,  $e$ , and the angle  $\theta$  (which is zero when the vector radius points toward apastron) as

$$\rho(\theta) = \frac{a(1 - e^2)}{1 - e \cos \theta} \quad (7)$$

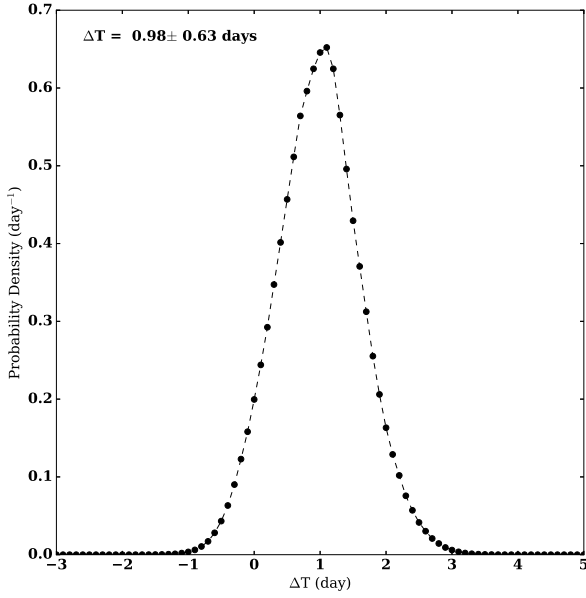


**Figure 6.** Probability density function for  $\Delta T$ . The PDF was calculated at steps of 0.1 d, shown with black dots connected by the dashed line.

The components of the vector radius in the  $[x', y']$  orbital plane, for an ellipse rotation of an angle  $\omega$ , are

$$\rho_{x'} = \frac{a(1 - e^2) \cos(\theta + \omega)}{1 - e \cos(\theta)} \quad (8)$$

$$\rho_{y'} = \frac{a(1 - e^2) \sin(\theta + \omega)}{1 - e \cos(\theta)} \quad (9)$$

In the plane perpendicular to the line-of-sight, owing to a rotation of an angle  $\zeta$  around  $[y']$ , these components become

$$x'' = \rho_{x'} \cos \zeta \quad y' = \rho_{y'}. \quad (10)$$

and, in the system of reference  $[x, y]$ ,

$$x_{orbit} = x'' \cos w - y' \sin w \quad (11)$$

$$y_{orbit} = y' \cos w + x'' \sin w \quad (12)$$

where  $w = \hat{M}\hat{A}\hat{W} = \hat{M}\hat{O}\hat{W}$  in Fig. 8 is a free angle, to be determined by the fit (see Sec. 5.3).

## 5.2 The jet precession motion

We assume the jet geometry and properties as described in [Massi & Torricelli-Ciamponi \(2014\)](#). In Fig. 9 the base of the jet is at point  $C$ . The jet base will be projected at a distance  $BF = BC \sin \eta = x_0 \sin \eta$ , where  $\eta$  is the angle the jet makes with the line-of-sight and  $x_0$  (i.e.,  $BC$  in Fig. 9) is the position of the jet base. Hence, for a thin jet, the components of the emitting region with respect to the plane perpendicular to the line of sight are

$$x_j = x_0 \sin \eta \cos(\delta + w) \quad y_j = x_0 \sin \eta \sin(\delta + w), \quad (13)$$

where the angle  $\delta$  can be derived from the spherical triangle  $ACG$  (see Fig. 9) as

$$\sin \delta \sin \eta = \sin \Omega \sin \psi \quad (14)$$

$$\cos \delta \sin \eta = \frac{\cos \psi - \cos \eta \cos \zeta}{\sin \zeta}, \quad (15)$$

and the angle  $\Omega$ , which changes because of precession, is defined as

$$\Omega = 2\pi t / P_2. \quad (16)$$

## 5.3 The total motion: results

Since the jet is anchored to the accretion disk of the compact object, the generic coordinate of the jet emitting plasma with respect to the assumed center of coordinates of Fig. 8 will be

$$X = l x_j + x_{orbit} \quad Y = l y_j + y_{orbit} \quad (17)$$

where  $l$  specifies the position along the jet of the peak radio flux; For an optically thin jet  $l = 1$ , while for an optically thick jet  $l$  is the position of optical depth unity. The value of  $l$  needs to be computed at each orbital phase in order to derive the correct coordinates  $(x, y)$  of the radio emission.

The resulting positions for the model astrometry are shown in Fig. 10. We use a physical model, i.e., the number of relativistic electrons injected every period  $P_1$  in a conical jet at a particular orbital phase, as found by [Massi & Torricelli-Ciamponi \(2014\)](#), who fitted 6.7 yr of Green Bank Interferometer radio data. With astrometric position, we can now better constrain the geometrical parameters of the model; i.e.,  $\psi$ , the jet angle to its precession axis and  $\xi$ , the jet opening angle. The angle  $\zeta$  is set to 25 degrees, which is the measured angle of the rotation axis of the Be star ([Nagae et al. 2006](#)), assuming the star spin axis is parallel to the orbital axis. The parameter  $w$ , that translates and rotates the trajectory in space without changing its shape is  $w = 230$  degrees. The model for the astrometric data shown in Fig. 10 result in a jet angle to its precession axis of  $\psi = 21$  degrees and a jet opening angle  $\xi = 6$  degrees. We note that these two angles for LS I +61°303 are similar to those of the well-studied precessing jet system SS 433; SS 433 has a half precessing cone angle of 20 deg and a jet opening angle of 5 deg ([Margon et al. 1979](#); [Paragi et al. 1999](#)).

Since our physical model assumes a steady jet, any transient emission, e.g., observation E in 2006 ([Massi et al. 2012](#)), cannot be used in the fits. For all other observations in 2006 the data and model overlap to within  $\pm 3\sigma$ . The same occurs for 2015, except for observation A. The model is able to reproduce the main feature of the observed ellipse, i.e. the non-uniform motion of the core with time, as seen in the middle panels of Fig. 10. For the 2006 observations, which were taken regularly every 3–4 d, the jet base (large squares) follows a regular path. The positions of the core (at  $\tau = 1$ ) for A, H, I and G are displaced by the jet base and just overlap with the edge of their related squares. The same occurs in the 2016 session, where the predicted core positions for A, B, H, and I are offset from the observed peaks. As shown in the bottom panels of Fig. 10, for these observations the angle between jet and the line of sight is small, below 21 degrees. Possibly the longer path of the radiation within the jet causes the higher optical depth (see Fig. A1 in [Massi & Torricelli-Ciamponi 2014](#))

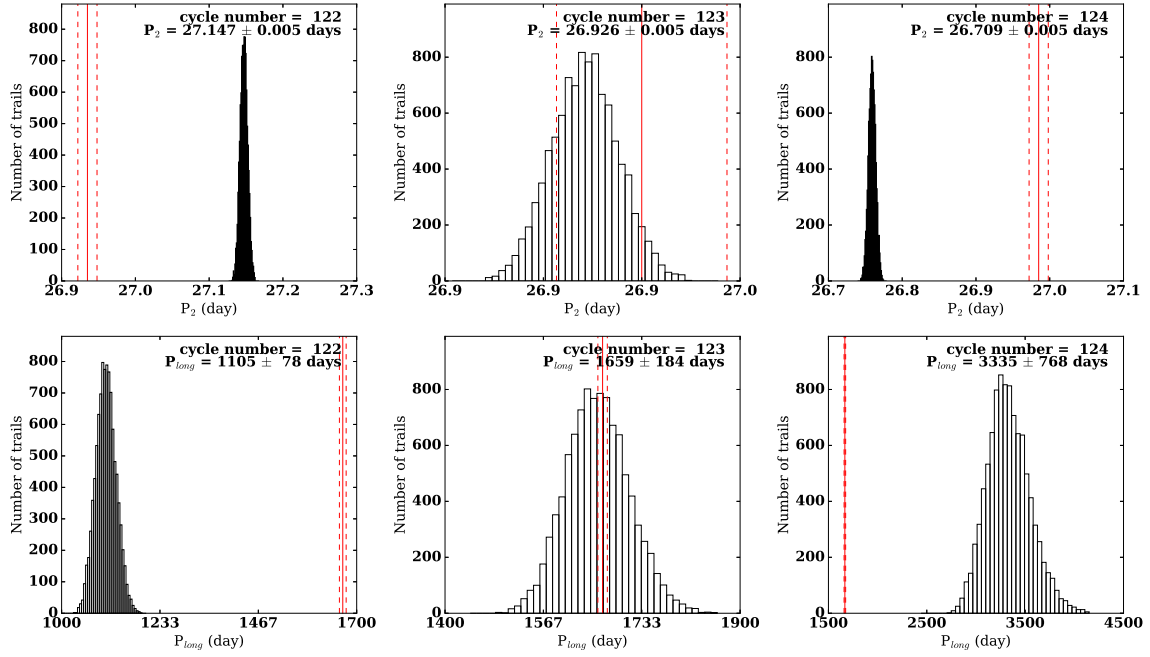


**Figure 7.** *Top panels* : Histograms of  $P_2$  estimated via Monte Carlo simulation, by adopting  $\Delta T = 0.98 \pm 0.63$  d, with cycle number = 122, 123 and 124 (top left, top middle and top right panels). We ran 10000 trials to estimate the value and  $1\sigma$  error of  $P_2$ . *Bottom panels* : Histograms of  $P_{long}$  estimated with relationship of  $P_{long} = P_1 \times P_2 / (P_2 - P_1)$ , by adopting  $P_1 = 26.496 \pm 0.013$  d (Massi & Torricelli-Ciamponi 2016), and  $P_2$  values from top panel estimations. Red solid and dashed vertical lines in top and bottom panels denote values and  $1\sigma$  errors of  $P_2$  and  $P_{long}$  estimated by Massi & Torricelli-Ciamponi (2016) and Gregory (2002) with Lomb-Sargle method, respectively.

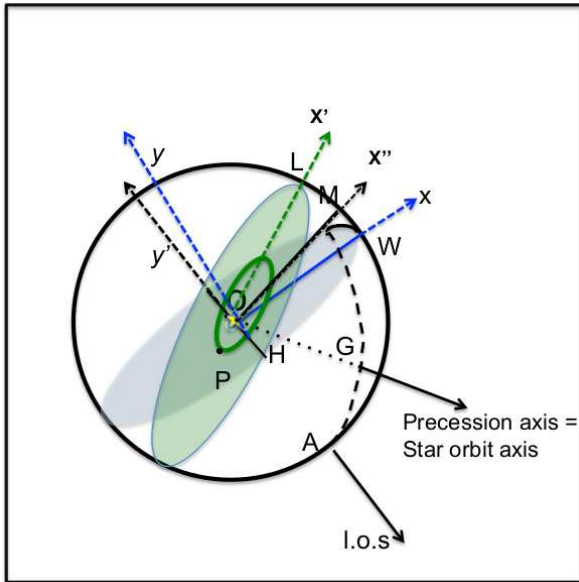


**Figure 8.** Geometry of the orbit. The real orbital plane is in green; the grey plane is perpendicular to the observer. The center of mass of the system is located at O;  $W\hat{O}L = \zeta$  is the angle between the orbital plane and the plane perpendicular to the line of sight;  $\omega = 90^\circ - P\hat{O}H$  and  $M\hat{O}W = w$ .

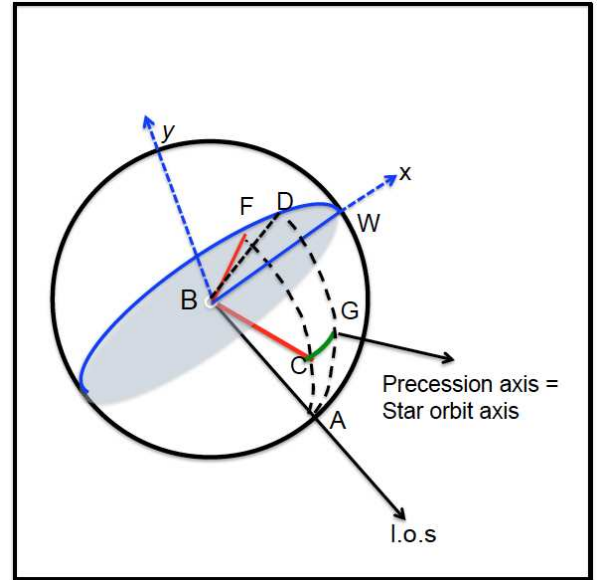


**Figure 9.** Geometry of the precessing radio jet.  $BC$  is the distance of the jet base ( $x_0$ ) from the compact object (located in  $B$ );  $BF$  is the projection of  $BC$  on the plane perpendicular to the line of sight;  $CA = \eta$ ;  $CG = \psi$ ;  $AG = \zeta$ ;  $C\hat{G}A = \Omega$ ;  $F\hat{B}D = C\hat{A}G = \delta$ ;  $D\hat{A}W = D\hat{B}W = w$  free angle to be determined.

## 6 PROPER MOTION AND 3D MOTION

Our observations also provide an accurate proper motion for LS I +61°303 as is evident in Figure 4. We find eastward and northward motions of  $\mu_\alpha = -0.150 \pm 0.006$  mas yr<sup>-1</sup>,  $\mu_\delta = -0.264 \pm 0.006$  mas yr<sup>-1</sup>, base on a time span of 3311 d be-

tween the 2006 and 2015 observations. For comparison, the proper motions of LS I +61°303 measured by *Hipparcos* (Hoogerwerf & Blaauw 2000) and *GAIA* (Data Release 1, Arenou et al. 2017) are  $[0.62 \pm 1.95, 1.63 \pm 1.75]$  mas yr<sup>-1</sup> and  $[-0.354 \pm 0.267, -0.077 \pm 0.211]$  mas yr<sup>-1</sup>, respectively. Boboltz et al. (2003) mea-

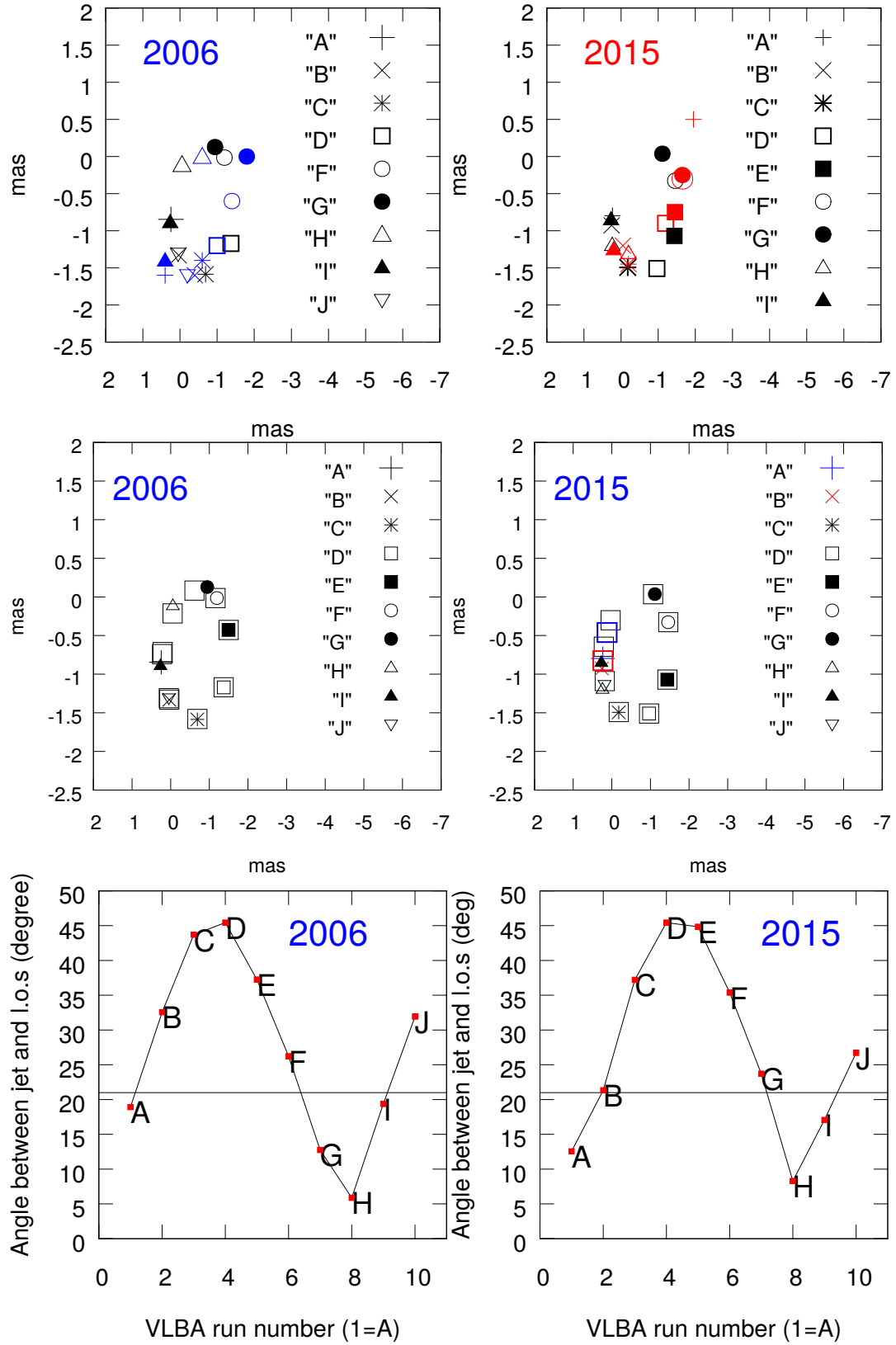


**Figure 10.** Top-panels: Model-data comparisons. The blue and red points are from VLBA astrometry in 2006 and 2015, respectively. The same symbols in black are used for the model data. Middle panels: Comparison of positions of the jet base (squares) and jet peak. Bottom panel: angle between the jet and the line of sight (see Section 5.3).

sured the proper motions of  $[0.97 \pm 0.26 -1.21 \pm 0.32]$  mas yr<sup>-1</sup> with Very Large Array (VLA) data. Except for the Boboltz et al values, previous estimates are consistent with our results. But, of course, our measurements have orders of magnitude better accuracy.

Assuming a distance of  $2.0 \pm 0.3$  kpc and  $V_{LSR} = 41.4 \pm 10$  km s<sup>-1</sup> (Aragona et al. 2009), we can estimate the full space velocity of the system. Adopting the distance to the Galactic center of  $8.34 \pm 0.16$  kpc, a Persic et al. (1996) universal rotation curve with a circular rotation speed at the Sun of  $240 \pm 8$  km s<sup>-1</sup>, and solar motion components of  $U_{\odot} = 10.7 \pm 1.8$ ,  $V_{\odot} = 15.6 \pm 6.8$  km s<sup>-1</sup> and  $W_{\odot} = 8.9 \pm 0.9$  km s<sup>-1</sup> from Reid et al. (2014b), we find peculiar (non-circular) of motion components for LS I +61°303 of  $U = 10.8 \pm 8.8$  km s<sup>-1</sup>,  $V = -10.3 \pm 5.9$  km s<sup>-1</sup>,  $W = 5.2 \pm 0.4$  km s<sup>-1</sup>. This translates to a speed of only 16 km s<sup>-1</sup>.

Recent analysis of *swift* X-ray data suggest that LS I +61°303 is a black hole (Massi et al. 2017). Theoretically, stellar mass black holes might be formed through different channels, i.e. with or without natal kicks and with or without supernovae (SN) explosion. For example, GRO J1655-40, is a runaway black hole system with a peculiar speed of  $112 \pm 18$  km s<sup>-1</sup> (Mirabel et al. 2002). It may be formed after an SN explosion created a neutron star, followed by fall-back of ejected envelope and a secondary collapse (Israelian et al. 1999; Mirabel et al. 2002; Mirabel & Rodrigues 2003). Alternatively, the black hole may be formed directly with a large natal kick (Repetto et al. 2012). In contrast, the peculiar motions of the well studied black hole X-ray binaries, Cygnus X-1 and GRS 1915+105, have been measured to be only  $\approx 20$  km s<sup>-1</sup> (Reid et al. 2011, 2014a). Cygnus X-1 is believed to have been formed through direct collapse of a massive star (Fryer & Kalogera 2001; Mirabel & Rodrigues 2003). The similarly low peculiar motion (16 km s<sup>-1</sup>) of LS I +61°303 measured here suggest that it may also contain a black hole formed through direct collapse of a massive star.

## 7 CONCLUSIONS

Using multi-epoch VLBA observations of LS I +61°303 in 2015, we were able to map the elliptical trajectory its radio emission. The agreement between these maps and those from previous observations in 2006 suggests that the radio jet is stable over the nine year interval. We then aligned the precessing phase and estimated the precession period to  $P_2 = 26.926 \pm 0.005$  d, with a physical model that takes into account orbital motion, jet precessing and radiative transfer. In addition, the long time span between observations allow us to determine an accurate proper motion and, then, the full space motion of LS I +61°303. We find a small peculiar motion of 16 km s<sup>-1</sup> for the system, which favors a black hole formation by direct collapse instead of a supernova explosion.

## ACKNOWLEDGEMENTS

This work has made use of data from the European Space Agency (ESA) mission *Gaia* (<https://www.cosmos.esa.int/gaia>), processed by the *Gaia* Data Processing and Analysis Consortium (DPAC, <https://www.cosmos.esa.int/web/gaia/dpac/consortium>). Funding for the DPAC has been provided by national institutions, in particular the institutions participating in the *Gaia* Multilateral Agreement. We would like to thank Prof. X.D. Li from the Nanjing University for useful discussions.

We would like to thank the referee, Dr Benito Marcote, who carefully read the original draft and share valuable comments and suggestions that greatly improve the quality of this paper.

*Facilities:* VLBA

## REFERENCES

- Albert, J., Aliu, E., Anderhub, H., et al. 2009, *ApJ*, 693, 303  
Aragona, C., McSwain, M. V., Grundstrom, E. D., et al. 2009, *ApJ*, 698, 514  
Arenou, F., Luri, X., Babusiaux, C., et al. 2017, *A&A*, 599, A50  
Boboltz, D. A., Fey, A. L., Johnston, K. J., et al. 2003, *AJ*, 126, 484  
Bosch-Ramon, V., Paredes, J. M., Romero, G. E., & Ribó, M. 2006, *A&A*, 459, L25  
Casares, J., Ribas, I., Paredes, J. M., Martí, J., & Allende Prieto, C. 2005, *MNRAS*, 360, 1105  
Dhawan, V., Mioduszewski, A., & Rupen, M. 2006, in *VI Microquasar Workshop: Microquasars and Beyond*, 52.1  
Eikenberry, S. S., Cameron, P. B., Fierce, B. W., et al. 2001, *ApJ*, 561, 1027  
Fryer, C. L. & Kalogera, V. 2001, *ApJ*, 554, 548  
Gregory, P. C. 2002, *ApJ*, 575, 427  
Gregory, P. C. & Taylor, A. R. 1978, *Nature*, 272, 704  
Hoogerwerf, R. & Blaauw, A. 2000, *A&A*, 360, 391  
Israelian, G., Rebolo, R., Basri, G., Casares, J., & Martín, E. L. 1999, *Nature*, 401, 142  
Jaron, F., Torricelli-Ciamponi, G., & Massi, M. 2016, *A&A*, 595, A92  
Kaufman Bernadó, M. M., Romero, G. E., & Mirabel, I. F. 2002, *A&A*, 385, L10  
Kettenis, M., van Langevelde, H. J., Reynolds, C., & Cotton, B. 2006, in *Astronomical Society of the Pacific Conference Series*, Vol. 351, *Astronomical Data Analysis Software and Systems XV*, ed. C. Gabriel, C. Arviset, D. Ponz, & S. Enrique, 497  
Margon, B., Grandi, S. A., Stone, R. P. S., & Ford, H. C. 1979, *ApJ*, 233, L63  
Martí, J. & Paredes, J. M. 1995, *A&A*, 298, 151  
Massi, M., Jaron, F., & Hovatta, T. 2015, *A&A*, 575, L9  
Massi, M. & Kaufman Bernadó, M. 2009, *ApJ*, 702, 1179  
Massi, M., Migliari, S., & Chernyakova, M. 2017, *ArXiv e-prints*  
Massi, M., Ros, E., & Zimmermann, L. 2012, *A&A*, 540, A142  
Massi, M., Ros, E., Zimmermann, L., & Torricelli-Ciamponi, G. 2013, in *Astronomical Society of the Pacific Conference Series*, Vol. 470, 370  
*Years of Astronomy in Utrecht*, ed. G. Pugliese, A. de Koter, & M. Wijburg, 373  
Massi, M. & Torricelli-Ciamponi, G. 2014, *A&A*, 564, A23  
Massi, M. & Torricelli-Ciamponi, G. 2016, *A&A*, 585, A123  
Mirabel, I. F., Mignani, R., Rodrigues, I., et al. 2002, *A&A*, 395, 595  
Mirabel, I. F. & Rodrigues, I. 2003, *Science*, 300, 1119  
Mirabel, I. F. & Rodríguez, L. F. 1999, *ARA&A*, 37, 409  
Nagae, O., Kawabata, K. S., Fukazawa, Y., et al. 2006, *PASJ*, 58, 1015  
Paragi, Z., Vermeulen, R. C., Fejes, I., et al. 1999, *A&A*, 348, 910  
Paredes, J. M., Martí, J., Peracaula, M., & Ribó, M. 1997, *A&A*, 320, L25  
Pearson, T. J., Shepherd, M. C., Taylor, G. B., & Myers, S. T. 1994, in *Bulletin of the American Astronomical Society*, Vol. 26, *American Astronomical Society Meeting Abstracts*, 1318  
Persic, M., Salucci, P., & Stel, F. 1996, *MNRAS*, 281, 27  
Reid, M. J., McClintock, J. E., Narayan, R., et al. 2011, *ApJ*, 742, 83  
Reid, M. J., McClintock, J. E., Steiner, J. F., et al. 2014a, *ApJ*, 796, 2  
Reid, M. J., Menten, K. M., Brunthaler, A., et al. 2014b, *ApJ*, 783, 130  
Repetto, S., Davies, M. B., & Sigurdsson, S. 2012, *MNRAS*, 425, 2799  
Romero, G. E., Okazaki, A. T., Orellana, M., & Owocki, S. P. 2007, *A&A*, 474, 15  
Shepherd, M. C. 1997, in *Astronomical Society of the Pacific Conference Series*, Vol. 125, *Astronomical Data Analysis Software and Systems VI*, ed. G. Hunt & H. Payne, 77  
Taylor, A. R., Kenny, H. T., Spencer, R. E., & Tzioumis, A. 1992, *ApJ*, 395, 268

**Table 1.** Jet core positions and estimated orbital, precessing and beating phases for 2006 and 2015 sessions

Epoch	date year-mn-dy-hr-mm	$\Delta R.A. \times \cos(\text{Dec})$ (mas)	$\Delta \text{DEC.}$ (mas)	JD (day)	$\Phi(P_1)$	$\Phi(P_2)$	$\Phi(P_{\text{long}})$
A	2006-06-30-15-26	2.40	-0.60	2453917.143056	0.187	0.822	0.352
B	2006-07-03-15-13	1.60	-0.60	2453920.134028	0.300	0.934	0.354
C	2006-07-07-14-58	1.40	-0.40	2453924.123611	0.451	0.082	0.356
D	2006-07-11-13-42	1.00	-0.20	2453928.070833	0.600	0.228	0.358
E	2006-07-15-14-27	-0.20	-0.60	2453932.102083	0.752	0.378	0.361
F	2006-07-18-14-15	0.60	0.40	2453935.093750	0.865	0.489	0.363
G	2006-07-21-14-03	0.20	1.00	2453938.085417	0.978	0.600	0.364
H	2006-07-24-13-51	1.40	1.00	2453941.077083	0.091	0.711	0.366
I	2006-07-27-13-39	2.40	-0.40	2453944.068750	0.203	0.822	0.368
J	2006-07-30-13-28	1.80	-0.60	2453947.061111	0.316	0.934	0.370
A	2015-07-24-13-34	-7.45	-3.10	2457228.065278	0.147	0.784	0.345
B	2015-07-26-13-27	-5.55	-4.80	2457230.060417	0.222	0.858	0.346
C	2015-07-30-13-11	-5.70	-5.05	2457234.049306	0.372	0.007	0.349
D	2015-08-03-09-25	-6.70	-4.50	2457237.892361	0.517	0.149	0.351
E	2015-08-06-12-43	-6.95	-4.35	2457241.029861	0.636	0.266	0.353
F	2015-08-10-12-28	-7.15	-3.90	2457245.019444	0.786	0.414	0.355
G	2015-08-13-12-15	-7.15	-3.85	2457248.010417	0.899	0.525	0.357
H	2015-08-19-11-52	-5.70	-4.90	2457253.994444	0.125	0.747	0.361
I	2015-08-21-11-44	-5.30	-4.85	2457255.988889	0.200	0.821	0.362
J	2015-08-23-11-36	-4.85	-5.50	2457257.983333	0.276	0.895	0.363

**Note:** Orbital, precessing and long beating phases (turns) are estimated with formula  $\phi = [(t - t_0) \bmod P]/P$ , by using  $P_1 = 26.496$  d,  $P_2 = 26.926$  d and  $P_{\text{long}} = 1661$  d. The reference time  $t_0$  is JD 2 443 366.775 (Gregory 2002).